nature astronomy

Article

https://doi.org/10.1038/s41550-024-02410-9

Detections of interstellar aromatic nitriles 2-cyanopyrene and 4-cyanopyrene in TMC-1

Received: 30 June 2024

Accepted: 9 October 2024

Published online: 05 November 2024

Check for updates

Gabi Wenzel[1] ✉, Thomas H. Speak[2], P. Bryan Changala[3], Reace H. J. Willis[2], Andrew M. Burkhardt[4], Shuo Zhang[1], Edwin A. Bergin[5], Alex N. Byrne[1], Steven B. Charnley[6], Zachary T. P. Fried[1], Harshal Gupta[3,7], Eric Herbst[8], Martin S. Holdren[1], Andrew Lipnicky[9], Ryan A. Loomis[9], Christopher N. Shingledecker[10], Ci Xue[1], Anthony J. Remijan[9], Alison E. Wendlandt[1], Michael C. McCarthy[3], Ilsa R. Cooke[2] ✉ & Brett A. McGuire[1,9] ✉

Polycyclic aromatic hydrocarbons (PAHs) are among the most widespread compounds in the universe, accounting for up to ~25% of all interstellar carbon. Since most unsubstituted PAHs do not possess permanent electric dipole moments, they are invisible to radio astronomy. Constraining their abundances relies on the detection of polar chemical proxies, such as aromatic nitriles. Here we report the detection of 2-cyanopyrene and 4-cyanopyrene, isomers of the recently detected 1-cyanopyrene. We find that these isomers are present in an abundance ratio of ~2:1:2, which mirrors the number of equivalent sites available for CN addition. We conclude that there is evidence that the cyanopyrene isomers formed by direct CN addition to pyrene under kinetic control in hydrogen-rich gas at 10 K and discuss constraints on the H/CN ratio for PAHs in the Taurus molecular cloud (TMC-1). Our detections of the cyanopyrene isomers suggest that small PAHs like pyrene must be either formed in or transported to the cold interstellar medium, challenging assumptions about the origin and fate of PAHs in space.

Polycyclic aromatic hydrocarbons (PAHs) are the likely carriers of the unidentified infrared (UIR) bands that dominate the spectra of most galactic and extragalactic objects[1]. These bright features, specifically at 3.3, 6.2, 7.7, 8.6, 11.2 and 12.7 μm, are generally associated with vibrational modes of PAHs that undergo infrared (IR) fluorescence after having been electronically excited by absorbing far-ultraviolet photons[2,3]. In the astronomical objects where UIR bands are observed, PAHs are highly abundant (~10^{-7} relative to hydrogen[1]) and, therefore, critically impact the physics and chemistry of the interstellar medium (ISM). In particular, they play a key role in determining the ionization balance in molecular clouds, thus influencing ion–molecule chemistry[4] and contributing to the neutral gas heating due to the photoelectric effect[5]. Despite their perceived importance, little is known about the nature of individual PAH molecules in the ISM. While the presence and abundance of PAHs in space is strongly supported by IR observations using, for example, the Infrared Space Observatory[6], the Spitzer Space Observatory[7] and the recently launched James Webb Space Telescope[8], the spectra obtained in the mid-IR are a convolution of many different

[1]Department of Chemistry, Massachusetts Institute of Technology, Cambridge, MA, USA. [2]Department of Chemistry, University of British Columbia, Vancouver, British Columbia, Canada. [3]Center for Astrophysics | Harvard & Smithsonian, Cambridge, MA, USA. [4]Department of Earth, Environment, and Physics, Worcester State University, Worcester, MA, USA. [5]Department of Astronomy, University of Michigan, Ann Arbor, MI, USA. [6]Astrochemistry Laboratory, NASA Goddard Space Flight Center, Greenbelt, MD, USA. [7]Division of Astronomical Sciences, National Science Foundation, Alexandria, VA, USA. [8]Departments of Chemistry and Astronomy, University of Virginia, Charlottesville, VA, USA. [9]National Radio Astronomy Observatory, Charlottesville, VA, USA. [10]Department of Chemistry, Virginia Military Institute, Lexington, VA, USA. ✉e-mail: gwenzel@mit.edu; icooke@chem.ubc.ca; brettmc@mit.edu

hot PAH molecules that all contain similar functional groups. Due to this spectral congestion, identification of individual PAHs in the ISM has not yet been achieved using their vibrational fingerprints. However, comprehensive efforts to compare spectral variations across multiple astronomical objects have constrained the PAH families present in these astrophysical environments[9–11], including recently with unprecedented spatial resolution using the James Webb Space Telescope[8].

While extraterrestrial PAHs have been found in carbonaceous chondrites such as Murchison and Orgueil[12,13] and in samples returned from comet 81P/Wild 2 during the Stardust mission[14], their recent discovery in return samples from asteroid Ryugu shines new light on potential formation pathways[15,16]. Carbon-13 isotopic analysis of the PAHs found in Ryugu showed that the three-ring species such as anthracene and phenanthrene were formed at high temperatures (>1,000 K). Meanwhile, the two- and four-ring PAHs naphthalene, fluoranthene and pyrene (the most abundant PAH in Ryugu) must have formed via a kinetically controlled route at low temperatures (~10 K). Indeed, two- and four-ring PAHs have been unambiguously detected in the cold, dark Taurus molecular cloud (TMC-1) by radio astronomical observations[17–21].

In contrast to the hot, broad UIR bands, each molecule possessing a permanent dipole moment has a distinct rotational spectrum with narrow emission lines that can be observed using radio astronomy. Most PAHs considered in the literature are large (more than 30 carbon atoms), highly symmetric and unsubstituted ('pure' hydrocarbons) for which models predict a viable chance of survival under the harsh interstellar conditions[22]. However, due to their high symmetry, these PAHs often possess only a small or null dipole moment. Thus, despite their ubiquity, only five individual PAHs have been detected by radio astronomy so far[17–21]. The rotational emission from these unambiguously detected PAHs has been observed towards TMC-1 and originates from CN-functionalized PAHs (nitriles), with the exception of the asymmetric, pure PAH indene. It has been proposed that, owing to their large dipole moments, nitrile-substituted PAHs can be used as observational proxies for pure PAHs[23,24]. Extracting quantitative abundances of unsubstituted PAHs from these proxies, however, relies on knowledge of the kinetics of their dominant formation and destruction pathways[25].

Here, we present the interstellar detection of two additional CN-functionalized PAHs, 2-cyanopyrene and 4-cyanopyrene, isomers of the recently discovered 1-cyanopyrene, in TMC-1 using broadband radio astronomical observations and enhance the statistical evidence for their detections with a stacking and matched filtering analysis. The discovery of 2- and 4-cyanopyrene completes the set of all possible singly CN-substituted pyrene isomers, allowing us to explore their potential formation routes by comparing their abundances with each other and to further constrain the abundance of pure pyrene in TMC-1.

Results

Discovery of 2- and 4-cyanopyrene in TMC-1

The GOTHAM (Green Bank Telescope (GBT) Observations of TMC-1: Hunting Aromatic Molecules) project is a high-sensitivity high-spectral-resolution broadband line survey of TMC-1 with near-continuous coverage from approximately 8 to 36 GHz (ref. 26). The data were collected with the 100 m Robert C. Byrd GBT from 2018 to 2022[20,21,27].

First, the laboratory rotational spectra of pure samples of 2- and 4-cyanopyrene (see Fig. 1 for their structures) were measured between approximately 7 GHz and 18 GHz using a cavity-enhanced Fourier transform microwave (FTMW) spectrometer. To determine the rotational constants, 762 and 318 (individual or partly blended) transitions of 2-cyanopyrene and 4-cyanopyrene, respectively, were fitted to a standard asymmetric top rotational Hamiltonian (Methods). The derived spectroscopic constants, which are reported in Supplementary Table 1, allowed us to calculate the rotational rest transition frequencies up to ~25 GHz with an accuracy of ~ 2 kHz. Searches for the

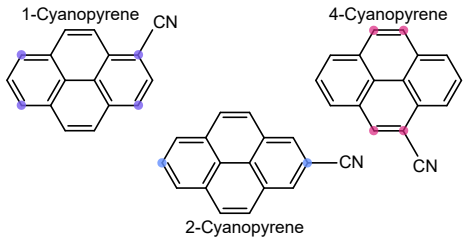

Fig. 1 | Structures of the cyanopyrene isomers. CN functionalization of pyrene ($C_{16}H_{10}$) forms three possible isomers ($C_{17}H_9N$), namely, 1-cyanopyrene (1-CN–$C_{16}H_9$), 2-cyanopyrene (2-CN–$C_{16}H_9$) and 4-cyanopyrene (4-CN–$C_{16}H_9$). Equivalent sites are shown with coloured circles.

radio emission features of 2- and 4-cyanopyrene towards TMC-1 were performed by simulating their rotational spectra under TMC-1 conditions (~5.8 km s^{-1}, 5–10 K) and comparing them with the GOTHAM data (Supplementary Fig. 1). Comparing the simulated rotational spectra with the root mean square (RMS) noise of our GOTHAM data depicted in Supplementary Fig. 1, we identify only a few spectral windows in which the 4-cyanopyrene features might be >1σ (above the noise, but ≤3σ, where σ is the standard deviation), while the 2-cyanopyrene lines are even weaker. These spectral windows are plotted in Supplementary Figs. 2 and 3 for 2-cyanopyrene and 4-cyanopyrene, respectively.

A Markov chain Monte Carlo (MCMC) analysis was used to derive the marginalized posterior parameters for the 2- and 4-cyanopyrene emission. These included the velocity in the local standard of rest, v_{lsr}, and column densities, N_T, in all four spatially separated velocity components of TMC-1 (ref. 28), a single excitation temperature, T_{ex}, and linewidth, ΔV. From this analysis, using the 1-cyanopyrene marginalized posterior parameters as priors (Methods, Supplementary Table 2 and ref. 21), we derived a column density of $0.84^{+0.09}_{-0.09} \times 10^{12}$ cm^{-2} at an excitation temperature of $7.90^{+0.53}_{-0.48}$ K for 2-cyanopyrene and $1.33^{+0.10}_{-0.09} \times 10^{12}$ cm^{-2} at $8.27^{+0.46}_{-0.44}$ K for 4-cyanopyrene (Supplementary Figs. 4 and 5 and Supplementary Table 3). The partition functions used for the MCMC analysis are listed in Supplementary Table 4.

To further explore the significance of our detections, we performed a velocity-stack and matched filtering analysis on both species[17,28]. For this purpose, spectral windows centred around the 150 brightest signal-to-noise ratio (SNR) lines of the simulated cyanopyrene spectra and the corresponding frequencies in the GOTHAM data were extracted in frequency space and collapsed into one SNR-weighted line in velocity space. Cross-correlating the latter stack (Fig. 2a,c, black) with the former (Fig. 2a,c, colour) yielded an impulse response for the two detections. The statistical significance of the 2-cyanopyrene and 4-cyanopyrene detections was 8.0σ and 12.9σ, respectively.

Discussion

Abundances of the cyanopyrene isomers

We extracted column densities of $1.52^{+0.18}_{-0.16}$, $0.84^{+0.09}_{-0.09}$ and $1.33^{+0.10}_{-0.09} \times 10^{12}$ cm^{-2} for the 1-cyanopyrene, 2-cyanopyrene and 4-cyanopyrene isomers, respectively, that is, a 1.8:1:1.6 abundance ratio (with an uncertainty of approximately ± 0.3) or roughly 2:1:2 (ref. 21). On the assumption that CN addition to a double bond in pyrene is the major formation pathway for the cyanopyrene isomers,

$$CN + C_{16}H_{10} \longrightarrow C_{16}H_9CN + H, \quad (1)$$

the observed ratio is consistent with two equivalent sites yielding 2-cyanopyrene and four equivalent sites yielding 1- and 4-cyanopyrene (Fig. 1, coloured circles).

The use of the cyanopyrene abundance to estimate the abundance of pyrene relies on knowledge of the formation pathway of cyanopyrene. If cyanopyrene is formed predominantly from CN addition to

https://doi.org/10.1038/s41550-024-02410-9

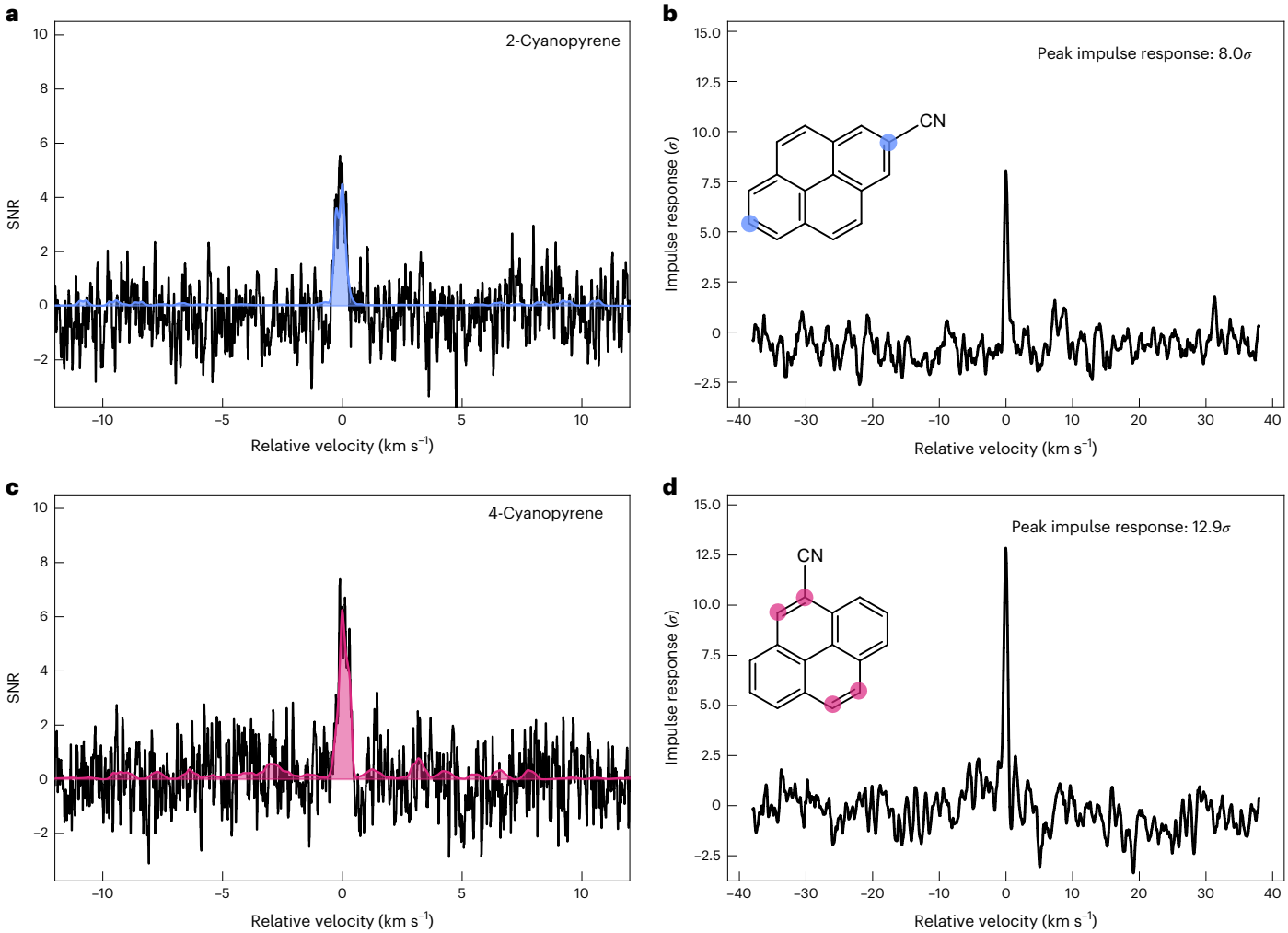

Fig. 2 | Velocity-stacked spectra and matched filter responses of 2- and 4-cyanopyrene. a,**c**, The stacked GOTHAM observations (black) are overlaid with the simulated stacked spectrum of 2-cyanopyrene (**a**) and 4-cyanopyrene (**c**) (blue and pink, respectively), each consisting of the 150 brightest SNR lines. Marginalized posterior parameters were used in both simulations, as reported in Supplementary Table 3. **b**,**d**, The corresponding impulse response for the matched filtering analysis is shown, yielding a significance of 8.0σ and 12.9σ for the 2-cyanopyrene (**b**) and 4-cyanopyrene detections (**d**), respectively. The small features in the stacked simulated spectrum (pink) in **c** result from the densely populated 4-cyanopyrene lines (Supplementary Figs. 1 and 3) that add up in the stack.

pyrene under kinetic control, then the relative cyanopyrene/pyrene abundance would be determined by the ratio of the CN addition rate and the total cyanopyrene destruction rate. In this case, it is reasonable to expect that the 1-, 2- and 4-cyanopyrene product-branching ratios would be proportional to the number of equivalent sites available for CN addition. Calculations of the CN addition rate coefficients were therefore carried out to evaluate whether the observed isomer distribution agrees with kinetic control for the addition of CN to pyrene (Methods and Supplementary Table 5).

The EP3-corrected ωB97X-D4/def2-TZVPP surface was incorporated into the energy-grained master equation calculator Master Equation Solver for Multi-Energy Well Reactions (MESMER) 7.0 (Supplementary Section 7). The site-specific bimolecular rate coefficients for the CN addition H elimination reaction with pyrene at 10 K were predicted to be $k_1 = 2.02 \times 10^{-10}$ cm^3 s^{-1}, $k_2 = 1.01 \times 10^{-10}$ cm^3 s^{-1} and $k_4 = 2.02 \times 10^{-10}$ cm^3 s^{-1}, consistent with the observation of the cyanopyrene isomers in a ~2:1:2 ratio. However, the product-branching ratios are sensitive to the heights of the submerged barriers for H elimination.

The heights of the submerged barriers on the EP3//ωB97X-D4/def2-TZVPP surface are large enough that, within the estimated uncertainty of the calculations, they could potentially impact the product distribution. Further computational work to evaluate the magnitude of the exit barriers will be important in elucidating whether the observed ratio of the cyanopyrene isomers agrees with a kinetically controlled addition of CN to pyrene.

In our previous work[21], we used a wide range (0.01–0.1) for the CN/H ratio to estimate the abundance of pyrene from 1-cyanopyrene. Here, we use astrochemical modelling, performed with the nautilus modelling code[29] (Methods) to further constrain the abundance of pyrene in TMC-1. While pyrene and cyanopyrene are not included in our models, chemically similar aromatics can be used to explore the CN/H ratio. In these models, we allow the rate coefficient for CN + aromatic (either indene or benzene) to vary, enabling us to determine how the CN/H ratio depends on the magnitude of the rate coefficient as well as the chemical age. We then used the outputs of the model (Fig. 3) and our predicted isomer-specific rate coefficients for CN + pyrene to estimate the expected CN/H ratio for cyanopyrene/pyrene in TMC-1. In addition, we compared the modelled CN/H ratio with the ratio of 2-cyanoindene/indene from radio observations[20].

Figure 3 shows the linear dependence of the CN/H ratio on the rate coefficient for the reaction of CN with an aromatic hydrocarbon, illustrated using 2-cyanoindene/indene, C_9H_7CN/C_9H_8, and

https://doi.org/10.1038/s41550-024-02410-9

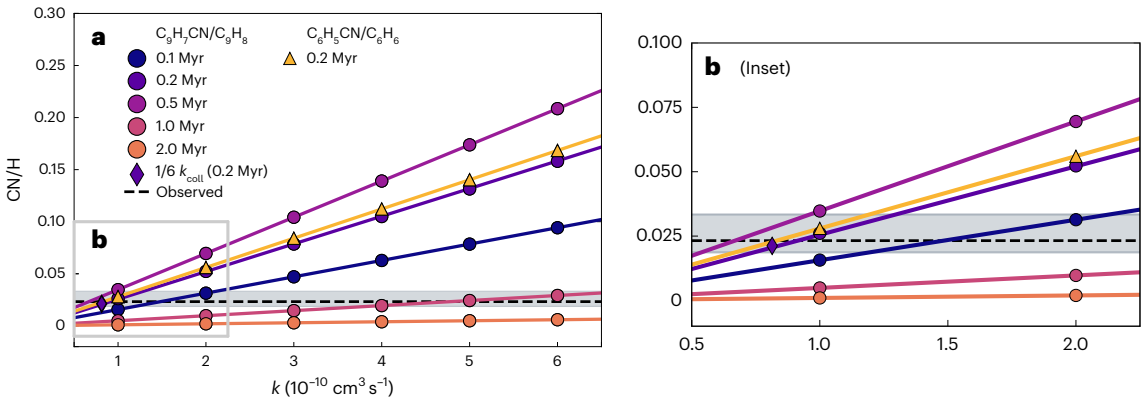

Fig. 3 | The CN/H ratio as a function of the CN+aromatic rate coefficient, *k*. **a**, The filled circles show ratios obtained from the astrochemical models for C_9H_7CN/C_9H_8 at different simulation ages. The isomer-specific CN/H ratio obtained at 0.2 Myr by taking 1/6 of the collision rate coefficient for the reaction of CN with indene (that is, 8.14×10^{-11} cm^3 s^{-1}) is shown by the purple diamond. The observed C_9H_7CN/C_9H_8 ratio is shown by the horizontal dashed line with uncertainties shown in the horizontal grey bar. The yellow-filled triangles show C_6H_5CN/C_6H_6 at 0.2 Myr as a function of the CN + C_6H_6 rate coefficient. **b**, Zoomed version of the area framed in grey in **a**.

benzonitrile/benzene, C_6H_5CN/C_6H_6. We explored this dependence for different chemical ages between 0.1 Myr and 2 Myr, since a range of values have been reported for different molecules and model parameters[28,30]. The linear dependence was observed for all chemical ages, albeit with different slopes. This trend is due to the increased efficiency of simultaneously destroying the pure aromatic and producing the nitrile-functionalized aromatic. Both benzene and indene display similar trends with their CN/H ratios nearly identical at 0.2 Myr. Assuming similar production and destruction mechanisms, these models can be extended to the CN/H ratio for other aromatic molecules and their nitriles, such as naphthalene and the cyanonaphthalene isomers.

It is important to note that, while CN addition to benzene produces only one isomer (benzonitrile), CN addition to a double bond in indene can occur via six distinct sites; therefore, the product-branching ratio must be taken into account when determining the appropriate CN + aromatic rate coefficient. To explore this in more detail, we estimated the CN + indene collision rate coefficient, k_{coll} (Methods and equation (3)). Using the simple assumption that each product channel is equally likely, $k_{coll}/6 = 8.14 \times 10^{-10}$ cm^3 s^{-1} is used to approximate the rate coefficient for CN + indene to form 2-cyanoindene in the collision limit. To compare with observations, we chose an age of 0.2 Myr based on the approximate chemical age of TMC-1 that was derived previously from modelling of carbon chains[31,32]. As shown in Fig. 3, this rate coefficient is consistent with both the modelled and observed CN/H ratio for 2-cyanoindene/indene of 0.023. We therefore used these results to constrain the CN/H ratio for cyanopyrene/pyrene.

Using the MESMER predicted rate coefficients, the abundance of pyrene can be estimated from Fig. 3 as ~20× the abundance of either 1-cyanopyrene or 4-cyanopyrene (CN/H ≈ 0.05), or ~40× the abundance of 2-cyanopyrene (CN/H ≈ 0.025), that is, a column density of ~3×10^{13} cm^{-2}.

Bottom-up versus top-down formation pathways

Measurements of ^{13}C isotopic substitutions in samples from asteroid Ryugu suggest that the two- and four-ring PAHs naphthalene, fluoranthene and pyrene probably formed in low-temperature interstellar environments[16]. However, the observed doubly ^{13}C substitutions for three-ring PAHs anthracene and phenanthrene, as well as pyrene in the carbonaceous chondrite Murchison, suggest they may have formed in high-temperature circumstellar envelopes of evolved stars. Alternatively, these results could be explained by a scenario where these species formed or were altered on the parent body of asteroid Ryugu and, hence, after solar system formation. If these small PAHs are formed in circumstellar envelopes, they must survive destruction by radiation and shocks in the diffuse ISM[33,34]. However, if this is the case, it is difficult to understand why only the three-ring PAHs survived passage through the diffuse ISM. Indeed, cursory searches for the three-ring PAHs 9-cyanoanthracene and 9-cyanophenanthrene, whose rotational spectra are known[35], in GOTHAM observations of TMC-1 have not yet been successful.

Various bottom-up mechanisms have been proposed to explain the formation pathways of PAHs in high-temperature environments, such as combustion systems[36] and circumstellar envelopes[37]. These mechanisms generally occur in two stages[36]: first-ring closure followed by growth through subsequent addition of aromatic rings. The most prominent of the latter is the hydrogen abstraction, acetylene (C_2H_2) addition (HACA) mechanism[36]. In this mechanism, hydrogen is first abstracted from an aromatic molecule (typically by a hydrogen atom), followed by addition to the radical site. A bottom-up HACA mechanism to pyrene has been proposed by ref. 37 involving the reaction of the 4-phenanthrenyl radical ($C_{14}H_9^{\bullet}$) with C_2H_2. However, the addition requires overcoming a barrier on the order of 10–20 kJ mol^{-1} (1,200–2,400 K equivalent temperature), prohibiting the HACA mechanism at the low temperatures of TMC-1 (ref. 38).

An alternative low-temperature mechanism for the bottom-up ring growth of PAHs has been proposed, the so-called hydrogen abstraction, vinylacetylene (C_4H_4) addition (HAVA) mechanism. Phenanthrene has been shown to form by the HAVA mechanism via the naphthyl radical[39]. Since the HAVA mechanism generally involves only submerged barriers, it can operate at low temperatures like those in dense molecular clouds. Recently, the reaction between the phenylethynyl radical ($C_6H_5CC^{\bullet}$) and benzene has been proposed as another viable bottom-up mechanism to form phenanthrene at low temperature[40]. However, vinylacetylene addition to the 4-phenanthrenyl radical is not expected to form pyrene[41]. While this mechanism may form vinylpyrene, it is one of the few HAVA mechanisms studied that possesses a barrier in the entrance channel, due to steric hindrance at the reaction site. Thus, a low-temperature bottom-up mechanism to pyrene has yet to be unveiled.

Top-down routes to smaller PAHs have also been explored, including the fragmentation of bulk amorphous carbon or graphite by collisions of dust grains or interstellar shocks[42,43]. The relative importance of top-down versus bottom-up chemistry is difficult to quantify, and most astrochemical models focus on the latter. A comparison between the abundances of pyrene and smaller aromatic molecules detected in TMC-1 thus far can provide clues about its formation pathways. The column density of benzonitrile is $1.73^{+0.85}_{-0.10} \times 10^{12}$ cm^{-2} (ref. 17); therefore, assuming a CN + benzene rate coefficient of ~4×10^{-10} cm^{-3} s^{-1}

(ref. 24), we predict a benzene abundance of ~1.4×10^{13} cm^{-2}. Since this is approximately half the abundance that we derive above for pyrene, it is difficult to envision a bottom-up route to pyrene from benzene, unless benzene is destroyed much more efficiently than pyrene. Observational constraints on the abundance of larger PAHs would help to constrain the relative importance of top-down versus bottom-up formation pathways. If pyrene does form top-down, further work is required to reconcile this mechanism with the isotopic results from Ryugu.

Conclusions

We report interstellar detections of the two CN-functionalized pyrene isomers, 2- and 4-cyanopyrene, in our GOTHAM observations towards the dark molecular cloud TMC-1. Together with the previously detected 1-cyanopyrene, they form a family of the largest interstellar molecules identified by radio astronomy so far. New theoretical calculations of the CN + pyrene rate coefficients and their column densities of $1.52^{+0.18}_{-0.16}$, $0.84^{+0.09}_{-0.09}$ and $1.33^{+0.10}_{-0.09} \times 10^{12}$ cm^{-2} for 1-cyanopyrene, 2-cyanopyrene and 4-cyanopyrene, respectively, forming an approximate abundance ratio of 2:1:2, help better constrain the CN/H ratio of all aromatic species present in TMC-1 and, hence, the abundance of pure pyrene. We estimate a column density for gas-phase pyrene of ~3×10^{13} cm^{-2} corresponding to an abundance of ~3×10^{-9} with respect to H_2. In light of this, PAH formation mechanisms should be revisited to help explain the origin and abundance of pyrene in TMC-1.

Methods

Rotational spectroscopy

Rotational spectra of 2- and 4-cyanopyrene were predicted using the open-source quantum chemical package PSI4 (ref. 44). Their geometries were initially optimized at the B3LYP/6-311++G(d,p)[45] level of theory and basis set and subsequently using M06-2X/6-31+G(d)[46,47], determining their rotational constants A, B and C as presented in Supplementary Table 1. They agree well with the constants derived by the 'Lego brick' approach[48]. The ^{14}N nuclear electric quadrupole hyperfine coupling constants, χ_{aa} and χ_{bb}, were estimated by rotating the χ tensor of benzonitrile (cyanobenzene), which has been accurately measured experimentally[49], to the principal axis coordinate systems of 2- and 4-cyanopyrene, assuming that the electric field gradients remain identical with respect to the local CN bond axis and molecular plane.

The laboratory rotational transition rest frequencies were measured using a cavity-enhanced FTMW spectrometer[50,51]. A laser ablation source was employed for solid sample introduction. The molecule of interest was either mixed with anthracene (Sigma-Aldrich, purity ≥97%) as a binder material in a 1:1 ratio to produce a homogeneous mixture (4-cyanopyrene) or used as is (2-cyanopyrene) and pressed with 3 tonnes of press force in a hydraulic press into a 0.25″-diameter cylindrical sample rod. The sample rod was mounted 8 mm downstream of a pulsed solenoid valve that was backed with 2.5 kTorr of neon as carrier gas. Sample ablation was performed using the second harmonic of a Continuum Surelite (SLI-10) Nd:YAG laser at a wavelength of 532 nm with a pulse energy of 50 mJ synchronized to operate during the ≤1 ms opening time of the solenoid valve. The ablated cyanopyrenes were carried into the FTMW spectrometer, and the supersonic expansion cooled them to a rotational temperature of ~2 K. After a brief search near the predicted frequencies of the strongest transitions, we observed several lines that could be successfully assigned to 2- and 4-cyanopyrene and were used to iteratively refine the spectroscopic predictions to search for additional transitions. Ultimately, we observed 762 and 318 individual or partly blended rotational transitions over the 7–16 GHz frequency range for 2-cyanopyrene and 4-cyanopyrene, respectively. The rest frequencies were least-squares fit to a standard rotational Hamiltonian using SPCAT/SPFIT in Pickett's CALPGM suite of programmes[52] (A-reduced, I^r representation) including quartic centrifugal distortion and ^{14}N nuclear electric quadrupole hyperfine coupling constants, which are reported in Supplementary Table 1.

Observations and analysis

Our analyses make use of data from the GOTHAM project[17,26] including observations up until May 2022[20,27]. Spectra were collected using the VErsatile GBT Astronomical Spectrometer (VEGAS) on the 100 m Robert C. Byrd GBT. Project codes for the observations used in the data set are AGBT17A_164, AGBT17A_434, AGBT18A_333, AGBT18B_007, AGBT19B_047, AGBT20A_516, AGBT21A_414 and AGBT21B_210. Data were recorded with a uniform frequency resolution of 1.4 kHz, or 0.05–0.01 km s^{-1} in velocity space.

The data span the X-, Ku- and K- and most of the Ka-receiver bands, with nearly continuous coverage from 7.9 to 11.6 GHz, 12.7 to 15.6 GHz and 18.0 to 36.4 GHz. The total bandwidth covered is 24.9 GHz. To visualize the spectral coverage, the GOTHAM dataset is overlaid in Supplementary Fig. 1 with the simulated rotational spectra of the cyanopyrene isomers at ~8 K. The cyanopyrene lines covered by the GOTHAM dataset are shown in violet (1-cyanopyrene), blue (2-cyanopyrene) and pink (4-cyanopyrene). The shaded grey boxes represent the averaged RMS noise level in each data chunk, typically ~2–20 mK. The RMS noise increase at higher frequencies is due to the shorter total integration times in those frequency ranges.

Pointing was performed on the cyanopolyyne peak in TMC-1 at right ascension $04^h41^m42^s.50$, declination $+25°41'26''.8$ (J2000 equinox). Spectra (on/off source) were collected using position-switching between the source and an emission-free position offset by 1°. Repointing and focusing were generally carried out every 1–2 h, primarily on the calibrator J0530+1331. Flux calibration was performed using an internal noise diode and Karl G. Jansky Very Large Array observations of J0530+1331, that is, the same source used for pointing. The flux uncertainty is estimated to be ~20% (refs. 20,27).

MCMC analysis

Prior observations of TMC-1 have shown that most centimetre-wave emission can be separated into contributions from four different velocity components[53–55]. Thus, we consider four different Doppler components, each with independent source size, velocity (in the local standard of rest, v_{lsr}) and column densities (N_T); and a shared uniform excitation temperature (T_{ex}) and linewidth (ΔV), resulting in 14 modelling parameters for each molecule.

To account for covariance between the model parameters, we use an affine-invariant MCMC sampling analysis, which has previously been applied to complex probability distributions in many components, including for previous observations of molecules[17,28].

The priors we adopted for the MCMC analysis of the two newly detected cyanopyrene isomers are listed in Supplementary Table 2. A uniform distribution (that is, unconstrained within the minima and maxima) was chosen for the N_T and T_{ex} priors, whereas the remaining parameters were set to have more tightly constrained Gaussian distributed priors centred at the values determined by prior observations of chemically similar species benzonitrile, cyanonaphthalenes[17] and 1-cyanopyrene[21].

Posterior probability distributions for each of the model parameters, along with their covariances, were generated using 100 walkers with 10,000 samples. The resulting source-dependent molecular parameters for the cyanopyrene isomers are reported in Supplementary Table 3. The covariance plots of the 14 parameters resulting from our MCMC analysis for the 2- and 4-cyanopyrene isomers are shown in Supplementary Figs. 4 and 5. The covariance plot for 1-cyanopyrene can be found in the supplementary material for ref. 21.

Theoretical calculations

Initial structures for the adducts and separated reagents were optimized with the RI-BP86 density functional theory (DFT) functional[56] using the def2-SVP basis set[57] and including D3(BJ) empirical dispersion corrections[58] (RI-BP86-D3(BJ)/def2-SVP will be referred to as DFT-Cheap). The presence of barriers to subsequent transfer and

elimination from the adducts was evaluated using relaxed surface scans with DFT-Cheap. Relaxed scans of the surface are carried out by allowing all but one coordinate within the molecule to reach their energy minimum while varying the fixed value of the frozen coordinate (typically a bond length). These scans were carried out in the forward and reverse directions to check for consistency. For example, in the case of CN addition to the ring, the coordinate scanned was the bond length between the ring carbon atom and the carbon of the CN radical. Where peaks in the energy profile for the relaxed scans were observed, these were used as the initial structure for transition state optimizations. All the structures calculated previously were then further refined and harmonic vibrations were calculated with the ωB97X functional[59] with the triple zeta basis set def2-TZVPP[60] and D4 empirical dispersion corrections[61] (henceforth DFT-2); intrinsic reaction coordinate scans were carried out to ensure that these structures connected to reactants and products using the ORCA implementation of the method of Morokuma and coworkers[62,63]. Harmonic vibrational frequencies were scaled by 0.95334 and harmonic zero point energies were scaled by 0.9779 in the manner suggested by ref. 64.

Single-point energy corrections were then carried out using the EP3 approximation of the CCSD(T) (coupled cluster theory with full treatment of single and double excitations and including perturbative treatment of triple excitations) complete basis set (CBS) limit[65,66]; this approximation is based on three MP2 (Møller–Plesset perturbation theory second-order treatment of electron correlation) calculations with increasing basis set size and a single CCSD(T) calculation with the smallest basis set (equation (2)). Here, the small basis set was Dunning's correlation consistent basis set cc-pVDZ with the extrapolation of the MP2 energies also using cc-pVTZ and cc-pVQZ[67]; these basis sets were taken from the correlation consistent basis set repository, ccREPO[68]. This approach can typically yield accuracy on the order of 5–15 kJ mol^{-1}. However, the accuracy of the relative energies of similar species, such as the three isomers of cyanopyrene formed, will probably be much higher on the order of ±1 kJ mol^{-1}. All calculations were performed using the open-source quantum chemical package ORCA 5.0.4 (ref. 63). As no barriers at the DFT-Cheap level had been observed for the addition of CN to the ring in the 1-, 2- or 4-position, additional relaxed scans with the more reliable hybrid functionals and triple zeta basis sets DFT-2 (refs. 59–61) and M06-2X/def2-TZVPP[46,60] were carried out to verify this result. The potential energy curves recovered from these relaxed scans for CN approach to the ring did not find any submerged barriers and pre-reaction complexes; as such, the influence of pre-reaction complexes on these routes was not considered.

$$\mathrm{CCSD(T)/CBS} \approx \mathrm{EP3} = E_{\mathrm{HFCBS}} + E_{\mathrm{MP2CBS}} + E_{\mathrm{CCSD(T)small}} - E_{\mathrm{MP2small}} \quad (2)$$

The results show that the approach of CN to pyrene is barrierless for the addition of carbon to the 1-, 2- or 4-positions, leading to the formation of deeply bound adducts 121–182 kJ mol^{-1} below the entrance energies. The barriers to the subsequent H atom elimination are submerged by 2–17 kJ mol^{-1}.

This EP3//DFT-2 surface was then incorporated into the energy-grained master equation calculator MESMER 7.0 (ref. 69), which allowed the reaction to be simulated over a range of densities (1×10^4 to 1×10^{15} cm^{-3}) and temperatures (10–300 K). There are eight equivalent pathways to addition at the 1- and 4-positions and four equivalent pathways to addition at the 2-position. The temperature-dependent collision rate coefficient for CN + pyrene was estimated using classical capture theory[70]

$$k_{\mathrm{coll}}(T) = \sigma_{\mathrm{coll}}\langle v(T)\rangle = \left[\pi\left(\frac{2C_6}{k_{\mathrm{B}}T}\right)^{1/3}\Gamma\left(\frac{2}{3}\right)\right]\left[\left(\frac{8k_{\mathrm{B}}T}{\pi\mu}\right)^{1/2}\right], \quad (3)$$

where k_{B} is the Boltzmann constant, $\Gamma(x)$ is the gamma function such that $\Gamma(2/3) = 1.353$, μ is the reduced mass of the collision and C_6 is the sum of coefficients describing the magnitude of the attractive forces between collision partners[71].

$$C_6 = \frac{2}{3}\left(\frac{\mu_1^2\mu_2^2}{k_{\mathrm{B}}T(4\pi\epsilon_0)^2}\right) + \frac{\mu_1^2\alpha_2 + \mu_2^2\alpha_1}{4\pi\epsilon_0} + \frac{3}{2}\alpha_1\alpha_2\left(\frac{I_1I_2}{I_1 + I_2}\right), \quad (4)$$

where ϵ_0 represents the permittivity of free space, μ_1 and μ_2 are the dipole moments of the reactants, and α_1/α_2 and I_1/I_2 are their polarizabilities and ionization energies, respectively. Where possible, these values were taken from the online databases National Institute of Standards and Technology Chemistry WebBook and Computational Chemistry Comparison and Benchmark Database[72,73]; where these were not available, they were calculated using DFT-2. This approach is generally accurate within a factor of 2 for the prediction of rate coefficients for neutral–neutral barrierless reactions[71].

The capture rate leading to an individual adduct was set to the fraction of the total number of pathways available that led to the formation of that isomer and the estimated overall capture rate. The redissociation of the adducts was then treated with the inverse Laplace transformation methodology[74] in MESMER along with Rice–Ramsperger–Kassel–Marcus treatment[75–77] for the H atom elimination reactions. Quantum mechanical tunnelling effects were accounted for using an asymmetric Eckart barrier model[78]. The impact of the size of the energy grains was evaluated by varying the grain sizes between 30 cm^{-1} and 5 cm^{-1} until the result had reached a consistent value.

The results of the MESMER simulations (for 10 K and 2×10^4 cm^{-3}) have been summarized in Supplementary Table 5. The primary route to product formation is via well-skipping. An estimate for the uncertainties in the barrier heights was accounted for by concertedly raising and lowering all three barriers by 10 kJ mol^{-1}. The predicted branching ratios are 2:1:2 for 1-, 2- and 4-cyanopyrene formation with an overall rate coefficient of 5.05×10^{-10} cm^3 s^{-1}.

Astrochemical models

To gain insights into the CN/H ratio in TMC-1, we adapted the three-phase chemical network model nautilus v1.1 code[29]. The reaction network is that of ref. 32, with modifications to the ion–neutral reaction rate coefficients as described below. We use the same initial conditions as described in ref. 79, that is, gas and dust temperatures of 10 K, gas densities of 2×10^4 cm^{-3} and a cosmic-ray ionization rate of 1.3×10^{-17} s^{-1}.

Initial elemental abundances were taken from ref. 80 with the exception of atomic oxygen, where we utilize a slightly carbon-rich C/O ≈ 1.1 and $X_0(t = 0) \approx 1.5 \times 10^{-4}$, as described in refs. 28,79.

Rate coefficients for the destruction of benzonitrile via ion–neutral reactions were updated (Supplementary Table 7), estimated assuming a Su–Chesnavich capture model to account for long-range Coulombic attractions[81,82]. In addition, the reaction of carbon atoms with benzene was added to the network for consistency with the other aromatics (indene and naphthalene) currently in the network.

$$\mathrm{C} + \mathrm{C_6H_6} \longrightarrow \mathrm{C_7H_5} + \mathrm{H} \quad (5)$$

The rate coefficient was initially set to 5×10^{-10} cm^3 s^{-1}, the room temperature value[83]. Modifying the rate coefficient of C + aromatic was found to strongly influence the absolute abundance of benzene, benzonitrile, indene and cyanoindene; however, it had negligible influence on the observed abundance ratios (≤4% for both benzonitrile/benzene and 2-cyanoindene/indene).

The rate coefficient for CN and indene was calculated using classical capture theory[70,71] to be 4.88×10^{-10} cm^3 s^{-1}; assuming equal formation of all isomers, this leads to a site-specific rate coefficient of 8.14×10^{-10} cm^3 s^{-1} for 2-cyanoindene.

To evaluate the sensitivity of the model predictions to the CN + aromatic rate coefficient, the model was run for a range of $k_{\mathrm{CN+benzene}}$

between 0.5×10^{-10} cm^3 s^{-1} and 6×10^{-10} cm^3 s^{-1} and for a range of $k_{CN+indene}$ between 0.81×10^{-10} cm^3 s^{-1} and 10×10^{-10} cm^3 s^{-1}. The observed ratios of benzonitrile/benzene and cyanoindene/indene depend linearly on their formation rate coefficient ($k_{CN+aromatic}$). As can be seen in Fig. 3, there is excellent agreement between the predicted ratio of cyanoindene to indene and benzonitrile to benzene using our updated reaction network. Furthermore, there is also a strong agreement with the observed isomer-specific ratio for 2-cyanoindene to indene.

Synthesis

Syntheses of 2- and 4-cyanopyrene were achieved using pyrene and hexahydropyrene as starting materials, respectively, as reported in the literature[84–89]. The synthetic routes to form these two cyanopyrene isomers are described in detail in Supplementary Section 9.

Data availability

All data from our observing programme GOTHAM are now available to the scientific community through the National Radio Astronomy Observatory and Green Bank Observatory archives at https://data.nrao.edu/portal/ under project codes AGBT17A_164, AGBT17A_434, AGBT18A_333, AGBT18B_007, AGBT19B_047, AGBT20A_516, AGBT21A_414 and AGBT21B_210. Calibrated and reduced observational data windowed around the reported transitions, the full catalogues of 2- and 4-cyanopyrene (including quantum numbers of each transition) and the partition functions used in the MCMC analysis are available via Zenodo at https://doi.org/10.5281/zenodo.13894479 (ref. 90).

References

1. Tielens, A. Interstellar polycyclic aromatic hydrocarbon molecules. *Annu. Rev. Astron. Astrophys.* **46**, 289–337 (2008).
2. Léger, A. & Puget, J. L. Identification of the 'unidentified' IR emission features of interstellar dust? *Astron. Astrophys.* **137**, L5–L8 (1984).
3. Allamandola, L. J., Tielens, A. G. G. M. & Barker, J. R. Polycyclic aromatic hydrocarbons and the unidentified infrared emission bands: auto exhaust along the Milky Way. *Astrophys. J.* **290**, L25–L28 (1985).
4. Bakes, E. L. O. & Tielens, A. G. G. M. The effects of polycyclic aromatic hydrocarbons on the chemistry of photodissociation regions. *Astrophys. J.* **499**, 258 (1998).
5. Berné, O., Foschino, S., Jalabert, F. & Joblin, C. Contribution of polycyclic aromatic hydrocarbon ionization to neutral gas heating in galaxies: model versus observations. *Astron. Astrophys.* **667**, A159 (2022).
6. Cernicharo, J. et al. Infrared Space Observatory's discovery of C_4H_2, C_6H_2, and benzene in CRL 618. *Astrophys. J.* **546**, L123–L126 (2001).
7. Li, A. Spitzer's perspective of polycyclic aromatic hydrocarbons in galaxies. *Nat. Astron.* **4**, 339–351 (2020).
8. Chown, R. et al. PDRs4All - IV. An embarrassment of riches: aromatic infrared bands in the Orion Bar. *Astron. Astrophys.* **685**, A75 (2024).
9. Peeters, E. et al. The rich 6 to 9 m spectrum of interstellar PAHs. *Astron. Astrophys.* **390**, 1089–1113 (2002).
10. Galliano, F., Madden, S. C., Tielens, A. G. G. M., Peeters, E. & Jones, A. P. Variations of the mid-IR aromatic features inside and among galaxies. *Astrophys. J.* **679**, 310–345 (2008).
11. Peeters, E. Astronomical observations of the PAH emission bands. *EAS Publ. Ser.* **46**, 13–27 (2011).
12. Sabbah, H. et al. Identification of PAH isomeric structure in cosmic dust analogs: the AROMA setup. *Astrophys. J.* **843**, 34 (2017).
13. Lecasble, M., Remusat, L., Viennet, J.-C., Laurent, B. & Bernard, S. Polycyclic aromatic hydrocarbons in carbonaceous chondrites can be used as tracers of both pre-accretion and secondary processes. *Geochim. Cosmochim. Acta* **335**, 243–255 (2022).
14. Clemett, S. J., Sandford, S. A., Nakamura-Messenger, K., Hörz, F., & McKay, D. S. Complex aromatic hydrocarbons in Stardust samples collected from comet 81P/Wild 2. *Meteorit. Planet. Sci.* **45**, 701–722 (2010).
15. Aponte, J. C. et al. PAHs, hydrocarbons, and dimethylsulfides in Asteroid Ryugu samples A0106 and C0107 and the Orgueil (CI1) meteorite. *Earth Planets Space* **75**, 28 (2023).
16. Zeichner, S. S. et al. Polycyclic aromatic hydrocarbons in samples of Ryugu formed in the interstellar medium. *Science* **382**, 1411–1416 (2023).
17. McGuire, B. A. et al. Detection of two interstellar polycyclic aromatic hydrocarbons via spectral matched filtering. *Science* **371**, 1265–1269 (2021).
18. Burkhardt, A. M. et al. Ubiquitous aromatic carbon chemistry at the earliest stages of star formation. *Nat. Astron.* **5**, 181–187 (2021).
19. Cernicharo, J. et al. Pure hydrocarbon cycles in TMC-1: discovery of ethynyl cyclopropenylidene, cyclopentadiene and indene. *Astron. Astrophys.* **649**, L15 (2021).
20. Sita, M. L. et al. Discovery of interstellar 2-cyanoindene (2-C9H7CN) in GOTHAM observations of TMC-1. *Astrophys. J. Lett.* **938**, L12 (2022).
21. Wenzel, G. et al. Detection of interstellar 1-cyanopyrene: a four-ring polycyclic aromatic hydrocarbon. *Science* **0**, eadq6391 (2024).
22. Montillaud, J., Joblin, C. & Toublanc, D. Evolution of polycyclic aromatic hydrocarbons in photodissociation regions—hydrogenation and charge states. *Astron. Astrophys.* **552**, A15 (2013).
23. Messinger, J. P., Gupta, D., Cooke, I. R., Okumura, M. & Sims, I. R. Rate constants of the CN + toluene reaction from 15 to 294 K and interstellar implications. *J. Phys. Chem. A* **124**, 7950–7958 (2020).
24. Cooke, I. R., Gupta, D., Messinger, J. P. & Sims, I. R. Benzonitrile as a proxy for benzene in the cold ISM: low-temperature rate coefficients for CN + C_6H_6. *Astrophys. J. Lett.* **891**, L41 (2020).
25. Balucani, N. et al. Formation of nitriles in the interstellar medium via reactions of cyano radicals, CN($X^2\Sigma^+$), with unsaturated hydrocarbons. *Astrophys. J.* **545**, 892 (2000).
26. McGuire, B. A. et al. Early science from GOTHAM: project overview, methods, and the detection of interstellar propargyl cyanide ($HCCCH_2CN$) in TMC-1. *Astrophys. J. Lett.* **900**, L10 (2020).
27. Cooke, I. R. et al. Detection of interstellar E-1-cyano-1,3-butadiene in GOTHAM observations of TMC-1. *Astrophys. J.* **948**, 133 (2023).
28. Loomis, R. A. et al. An investigation of spectral line stacking techniques and application to the detection of HC11N. *Nat. Astron.* **5**, 188–196 (2021).
29. Ruaud, M., Wakelam, V. & Hersant, F. Gas and grain chemical composition in cold cores as predicted by the Nautilus three-phase model. *Mon. Not. R. Astron. Soc.* **459**, 3756–3767 (2016).
30. Loison, J.-C., Wakelam, V., Hickson, K. M., Bergeat, A. & Mereau, R. The gas-phase chemistry of carbon chains in dark cloud chemical models. *Mon. Not. R. Astron. Soc.* **437**, 930–945 (2014).
31. McGuire, B. A. et al. Detection of the aromatic molecule benzonitrile (c-C_6H_5CN) in the interstellar medium. *Science* **359**, 202–205 (2018).
32. Siebert, M. A. et al. CH_3-terminated carbon chains in the GOTHAM survey of TMC-1: evidence of interstellar CH_3C_7N. *Astrophys. J.* **924**, 21 (2022).
33. Micelotta, E. R., Jones, A. P. & Tielens, A. G. G. M. Polycyclic aromatic hydrocarbon processing in interstellar shocks. *Astron. Astrophys.* **510**, A36 (2010).
34. Micelotta, E. R., Jones, A. P. & Tielens, A. G. G. M. Polycyclic aromatic hydrocarbon processing by cosmic rays. *Astron. Astrophys.* **526**, A52 (2011).

35. McNaughton, D. et al. Laboratory rotational spectroscopy of cyano substituted polycyclic aromatic hydrocarbons. *Mon. Not. R. Astron. Soc.* **476**, 5268–5273 (2018).
36. Reizer, E., Viskolcz, B. & Fiser, B. Formation and growth mechanisms of polycyclic aromatic hydrocarbons: a mini-review. *Chemosphere* **291**, 132793 (2022).
37. Zhao, L. et al. Pyrene synthesis in circumstellar envelopes and its role in the formation of 2D nanostructures. *Nat. Astron.* **2**, 413–419 (2018).
38. Kaiser, R. I. & Hansen, N. An aromatic universe—a physical chemistry perspective. *J. Phys. Chem. A* **125**, 3826–3840 (2021).
39. Zhao, L. et al. Low-temperature formation of polycyclic aromatic hydrocarbons in Titan's atmosphere. *Nat. Astron.* **2**, 973–979 (2018).
40. Goettl, S. J. et al. Exploring the chemical dynamics of phenanthrene ($C_{14}H_{10}$) formation via the bimolecular gas-phase reaction of the phenylethynyl radical (C_6H_5CC) with benzene (C_6H_6). *Faraday Discuss.* **251**, 509–522 (2024).
41. Zhao, L. et al. Gas phase synthesis of [4]-helicene. *Nat. Commun.* **10**, 1510 (2019).
42. Scott, A., Duley, W. W. & Pinho, G. P. Polycyclic aromatic hydrocarbons and fullerenes as decomposition products of hydrogenated amorphous carbon. *Astrophys. J.* **489**, L193 (1997).
43. Merino, P. et al. Graphene etching on SiC grains as a path to interstellar polycyclic aromatic hydrocarbons formation. *Nat. Commun.* **5**, 3054 (2014).
44. Smith, D. G. A. et al. Psi4 1.4: open-source software for high-throughput quantum chemistry. *J. Chem. Phys.* **152**, 184108 (2020).
45. Becke, A. D. Density-functional thermochemistry. III. The role of exact exchange. *J. Chem. Phys.* **98**, 5648–5652 (1993).
46. Zhao, Y. & Truhlar, D. G. The M06 suite of density functionals for main group thermochemistry, thermochemical kinetics, noncovalent interactions, excited states, and transition elements: two new functionals and systematic testing of four M06-class functionals and 12 other functionals. *Theor. Chem. Acc.* **120**, 215–241 (2008).
47. Lee, K. L. K. & McCarthy, M. Bayesian analysis of theoretical rotational constants from low-cost electronic structure methods. *J. Phys. Chem. A* **124**, 898–910 (2020).
48. Ye, H., Alessandrini, S., Melosso, M. & Puzzarini, C. Exploiting the 'Lego brick' approach to predict accurate molecular structures of PAHs and PANHs. *Phys. Chem. Chem. Phys.* **24**, 23254–23264 (2022).
49. Wohlfart, K., Schnell, M., Grabow, J.-U. & Küpper, J. Precise dipole moment and quadrupole coupling constants of benzonitrile. *J. Mol. Spectrosc.* **247**, 119–121 (2008).
50. Grabow, J.-U., Palmer, E. S., McCarthy, M. C. & Thaddeus, P. Supersonic-jet cryogenic-resonator coaxially oriented beam-resonator arrangement Fourier transform microwave spectrometer. *Rev. Sci. Instrum.* **76**, 093106 (2005).
51. Crabtree, K. N. et al. Microwave spectral taxonomy: a semi-automated combination of chirped-pulse and cavity Fourier-transform microwave spectroscopy. *J. Chem. Phys.* **144**, 124201 (2016).
52. Pickett, H. M. The fitting and prediction of vibration–rotation spectra with spin interactions. *J. Mol. Spectrosc.* **148**, 371–377 (1991).
53. Dobashi, K. et al. Spectral tomography for the line-of-sight structures of the Taurus Molecular Cloud 1. *Astrophys. J.* **864**, 82 (2018).
54. Dobashi, K. et al. Discovery of CCS velocity-coherent substructures in the Taurus Molecular Cloud 1. *Astrophys. J.* **879**, 88 (2019).
55. Xue, C. et al. Detection of interstellar HC_4NC and an Investigation of isocyanopolyyne chemistry under TMC-1 conditions. *Astrophys. J. Lett.* **900**, L9 (2020).
56. Lee, C., Yang, W. & Parr, R. G. Development of the Colle–Salvetti correlation-energy formula into a functional of the electron density. *Phys. Rev. B* **37**, 785–789 (1988).
57. Weigend, F. & Ahlrichs, R. Balanced basis sets of split valence, triple zeta valence and quadruple zeta valence quality for H to Rn: design and assessment of accuracy. *Phys. Chem. Chem. Phys.* **7**, 3297–3305 (2005).
58. Grimme, S., Ehrlich, S. & Goerigk, L. Effect of the damping function in dispersion corrected density functional theory. *J. Comput. Chem.* **32**, 1456–1465 (2011).
59. Chai, J.-D. & Head-Gordon, M. Systematic optimization of long-range corrected hybrid density functionals. *J. Chem. Phys.* **128**, 084106 (2008).
60. Weigend, F. Accurate Coulomb-fitting basis sets for H to Rn. *Phys. Chem. Chem. Phys.* **8**, 1057–1065 (2006).
61. Caldeweyher, E., Bannwarth, C. & Grimme, S. Extension of the D3 dispersion coefficient model. *J. Chem. Phys.* **147**, 034112 (2017).
62. Ishida, K., Morokuma, K. & Komornicki, A. The intrinsic reaction coordinate. *J. Chem. Phys.* **66**, 2153–2156 (1977).
63. Neese, F. Software update: the ORCA program system—version 5.0. *Wiley Interdiscip. Rev. Comput. Mol. Sci.* **12**, e1606 (2022).
64. Kesharwani, M. K., Brauer, B. & Martin, J. M. L. Frequency and zero-point vibrational energy scale factors for double-hybrid density functionals (and other selected methods): can anharmonic force fields be avoided? *J. Phys. Chem. A* **119**, 1701–1714 (2015).
65. Jurečka, P., Šponer, J., Černý, J. & Hobza, P. Benchmark database of accurate (MP2 and CCSD(T) complete basis set limit) interaction energies of small model complexes, DNA base pairs, and amino acid pairs. *Phys. Chem. Chem. Phys.* **8**, 1985–1993 (2006).
66. Liakos, D. G. & Neese, F. Improved correlation energy extrapolation schemes based on local pair natural orbital methods. *J. Phys. Chem. A* **116**, 4801–4816 (2012).
67. Dunning, T. H. Jr Gaussian basis sets for use in correlated molecular calculations. i. The atoms boron through neon and hydrogen. *J. Chem. Phys.* **90**, 1007–1023 (1989).
68. Hill, G. ccRepo. *Grant Hill* http://www.grant-hill.group.shef.ac.uk/ccrepo/index.html (2016).
69. Glowacki, D. R., Liang, C.-H., Morley, C., Pilling, M. J. & Robertson, S. H. MESMER: an open-source master equation solver for multi-energy well reactions. *J. Phys. Chem. A* **116**, 9545–9560 (2012).
70. Georgievskii, Y. & Klippenstein, S. J. Long-range transition state theory. *J. Chem. Phys.* **122**, 194103 (2005).
71. West, N. A. et al. Measurements of low temperature rate coefficients for the reaction of CH with CH_2O and application to dark cloud and AGB stellar wind models. *Astrophys. J.* **885**, 134 (2019).
72. Linstrom, P. & Mallard, W. NIST Chemistry WebBook, NIST standard reference database number 69. *NIST* https://doi.org/10.18434/T4D303 (2024).
73. Johnson, R. I. NIST computational chemistry comparison and benchmark database. *NIST* http://cccbdb.nist.gov/ (2022).
74. Davies, J. W., Green, N. J. B. & Pilling, M. J. The testing of models for unimolecular decomposition via inverse laplace transformation of experimental recombination rate data. *Chem. Phys. Lett.* **126**, 373–379 (1986).
75. Holbrook, K. A., Pilling, M. J., Robertson, S. H. & Robinson, P. J. *Unimolecular Reactions* (Wiley, 1996).
76. Baer, T. & Hase, W. L. *Unimolecular Reaction Dynamics: Theory and Experiments* (Oxford Univ. Press, 1996).

77. Lourderaj, U. & Hase, W. L. Theoretical and computational studies of non-RRKM unimolecular dynamics. *J. Phys. Chem. A* **113**, 2236–2253 (2009).
78. Miller, W. H. Tunneling corrections to unimolecular rate constants, with application to formaldehyde. *J. Am. Chem. Soc.* **101**, 6810–6814 (1979).
79. Burkhardt, A. M. et al. Discovery of the pure polycyclic aromatic hydrocarbon indene (c-C_9H_8) with GOTHAM observations of TMC-1. *Astrophys. J. Lett.* **913**, L18 (2021).
80. Hincelin, U. et al. Oxygen depletion in dense molecular clouds: a clue to a low O_2 abundance? *Astron. Astrophys.* **530**, A61 (2011).
81. Su, T. & Chesnavich, W. J. Parametrization of the ion–polar molecule collision rate constant by trajectory calculations. *J. Chem. Phys.* **76**, 5183–5185 (1982).
82. Woon, D. E. & Herbst, E. Quantum chemical predictions of the properties of known and postulated neutral interstellar molecules. *Astrophys. J. Suppl. Ser.* **185**, 273 (2009).
83. Haider, N. & Husain, D. Kinetic investigation of the collisional behavior of ground state atomic carbon, C(2p2(3PJ)), with halogenated olefins and aromatic compounds studied by time-resolved atomic resonance absorption spectroscopy in the vacuum ultra-violet. *Int. J. Chem. Kinet.* **25**, 423–435 (1993).
84. Wang, X. et al. Pyrene-based aggregation-induced emission luminogens (AIEgens) with less colour migration for anti-counterfeiting applications. *J. Mater. Chem. C* **9**, 12828–12838 (2021).
85. Đorđević, L., Milano, D., Demitri, N. & Bonifazi, D. O-annulation to polycyclic aromatic hydrocarbons: a tale of optoelectronic properties from five- to seven-membered rings. *Org. Lett.* **22**, 4283–4288 (2020).
86. Biswas, K. et al. On-surface synthesis of non-benzenoid nanographenes embedding azulene and Stone–Wales topologies. *Angew. Chem. Int. Ed.* **63**, e202318185 (2024).
87. Ji, L., Lorbach, A., Edkins, R. M. & Marder, T. B. Synthesis and photophysics of a 2,7-disubstituted donor–acceptor pyrene derivative: an example of the application of sequential Ir-catalyzed C–H borylation and substitution chemistry. *J. Org. Chem.* **80**, 5658–5665 (2015).
88. Lu, Q. et al. Comparison study of the site-effect on regioisomeric pyridyl–pyrene conjugates: synthesis, structures, and photophysical properties. *J. Org. Chem.* **85**, 4256–4266 (2020).
89. Bao-Xi, M., Li-Fang, Z. & Yun, Z. Crystal structure of pyrene-4-aldehyde, $C_{17}H_{10}O$. *Z. Kristallogr. NCS* **234**, 173–175 (2019).
90. Wenzel, G., Cooke, I., McGuire, B., & GOTHAM Collaboration. Detections of interstellar aromatic nitriles 2-cyanopyrene and 4-cyanopyrene in TMC-1 [Data set]. *Zenodo* https://doi.org/10.5281/zenodo.13894479 (2024).

Acknowledgements

The National Radio Astronomy Observatory is a facility of the National Science Foundation operated under cooperative agreement by Associated Universities, Inc. The Green Bank Observatory is a facility of the National Science Foundation operated under cooperative agreement by Associated Universities, Inc. G.W. and B.A.M. acknowledge the support of the Arnold and Mabel Beckman Foundation Beckman Young Investigator Award. Z.T.P.F., M.S.H. and B.A.M. acknowledge support from the Schmidt Family Futures Foundation. A.M.B. was supported in part by the Aisiku Summer Research Fellowship. A.N.B. acknowledges the support of NSF Graduate Research Fellowship (grant number 2141064). C.X. and B.A.M. acknowledge support of the National Science Foundation (grant number AST-2205126). I.R.C. acknowledges support from the Natural Sciences and Engineering Research Council of Canada (grant number RGPIN-2022-04684), the Canada Foundation for Innovation and the B.C. Knowledge Development Fund. P.B.C. and M.C.M. are supported by the National Science Foundation (grant number AST-2307137). S.B.C. is supported by the Goddard Center for Astrobiology and by the NASA Planetary Science Division Internal Scientist Funding Program through the Fundamental Laboratory Research work package (FLaRe). H.G. acknowledges support from the National Science Foundation for participation in this work as part of his independent research and development plan. Any opinions, findings and conclusions expressed in this material are those of the authors and do not necessarily reflect the views of the National Science Foundation.

Author contributions

All authors commented on and revised the manuscript. In addition, G.W. performed spectroscopic experiments, analysed observational data, conducted quantum chemical calculations and wrote the manuscript. T.H.S. performed quantum chemical calculations. H.G. performed spectroscopic experiments. I.R.C. analysed observational data and wrote the manuscript. P.B.C. performed spectroscopic experiments. E.A.B. analysed observational results. S.Z. performed the synthesis. A.M.B. performed observations. A.J.R. performed observations. C.X. performed observations. M.C.M. supervised laboratory experiments. A.E.W. supervised laboratory experiments. B.A.M. performed observations, analysed observational data, wrote the manuscript and designed the project.

Competing interests

The authors declare no competing interests.

Additional information

Supplementary information The online version contains supplementary material available at https://doi.org/10.1038/s41550-024-02410-9.

Correspondence and requests for materials should be addressed to Gabi Wenzel, Ilsa R. Cooke or Brett A. McGuire.

Peer review information *Nature Astronomy* thanks Ryan Fortenberry, Cristina Puzzarini and the other, anonymous, reviewer(s) for their contribution to the peer review of this work.